inorganics

MDPI

Article

Mo-Dopant-Enhanced Energy Storage Performance of VS_2 Microflowers as Electrode Materials for Supercapacitors

Jingwei Wang [1], Xuejun Zheng [1,2,*], Long Xie [1], Zhenhua Xiang [1] and Wenyuan He [1,3,*]

[1] School of Mechanical Engineering and Mechanics, Xiangtan University, Xiangtan 411105, China
[2] School of Electromechanical Engineering, Guangdong University of Technology, Guangzhou 510006, China
[3] School of Mechatronic Engineering and Automation, Foshan University, Foshan 528225, China
* Correspondence: zhengxuejun@xtu.edu.cn (X.Z.); hewenyuan@xtu.edu.cn (W.H.)

Abstract: It is found that Mo doping can enhance the supercapacitor performance of VS_2 microflowers. The X-ray diffraction combined with energy dispersive X-ray, X-ray photoelectron spectroscopy, and Raman spectra results verify the successful doping of Mo atoms into the VS_2 matrix. As the electrode material of supercapacitors, the Mo-doped VS_2 performs better electrochemical performance than pristine VS_2, achieving the specific capacitance of 170 F g^{-1} at 0.5 A g^{-1} and 389.5 F g^{-1} at 5 mV s^{-1}. Furthermore, the symmetric supercapacitor based on the Mo-doped VS_2 exhibits good stability and ideal rate capability. The enhanced capability is presumably ascribed to the more accessible active sites and faster electrons/ions diffusion kinetics, which are caused by the increased specific surface area, expanded interlayer spacing, and improved conductivity after Mo doping. This strategy can also be extended to strengthen the capacitive properties of other transition metal dichalcogenides for advanced energy storage devices.

Keywords: VS_2 microflowers; Mo doping; supercapacitors; electrode materials

check for updates

Academic Editor: Christian Julien

Received: 28 April 2025
Revised: 10 June 2025
Accepted: 11 June 2025
Published: 13 June 2025

Citation: Wang, J.; Zheng, X.; Xie, L.; Xiang, Z.; He, W. Mo-Dopant-Enhanced Energy Storage Performance of VS_2 Microflowers as Electrode Materials for Supercapacitors. *Inorganics* **2025**, *13*, 199. https://doi.org/10.3390/inorganics13060199

Copyright: © 2025 by the authors. Licensee MDPI, Basel, Switzerland. This article is an open access article distributed under the terms and conditions of the Creative Commons Attribution (CC BY) license (https://creativecommons.org/licenses/by/4.0/).

1. Introduction

Supercapacitors, holding superior power delivery, rapid rechargeability, and long cycle life, have drawn considerable attention in portable electronic devices and electric mass transit vehicles [1,2]. Based on the charge storage mechanisms, the supercapacitors are categorized into pseudo-capacitors (PCs) and electrical double-layer capacitors (EDLCs) [3,4]. Recently, transition metal dichalcogenides (TMDs), such as WS_2, MoS_2, etc. [5–7], have been utilized as supercapacitor electrode materials due to their larger interlayer spacing than graphene [8,9] and tunable material structure. VS_2 has garnered significant attention as EDLC electrode material owing to its intrinsic metallic nature and distinct layered structure, which offer a greater surface area and higher intrinsic fast ionic conductivity for double-layered charge storage [10,11]. Nevertheless, the application of pristine VS_2 in supercapacitors has been distinctly restricted by its mediocre specific capacity caused by its small ion-accessible surface area and limited electroconductivity [12,13]. To address these challenges, designing a particular nanostructured hollow multiple metal sulfide with excellent electrical conductivity and large surface area can demonstrate significant advantages for electrochemical performance [14–17]. Moreover, heteroatom doping is an additional practical strategy to raise the electrode activity of VS_2 [18,19].

It has been reported that doping can effectively tune the band gap, enhance the electron conductivity and charge transfer kinetics, generate more active sites, and therefore, boost the supercapacitor performance of TMDs (e.g., MoS_2, $MoSe_2$, etc.) [20–23]. From this perspective, it is also anticipated to observe the changes in various physiochemical

parameters (such as conductivity, porosity, and specific surface area) caused by doping heteroatoms in VS_2, which are the key factors determining supercapacitor performance. Nevertheless, there is currently no study on optimizing the physiochemical parameters of VS_2 by heteroatom doping to boost its supercapacitor performance. According to earlier theoretical estimates, Mo dopant may reduce the formation energy in VS_2, and the outermost electron configuration of Mo atoms is comparable to that of V atoms [24,25]. This implies that Mo doping may be a feasible way to boost the supercapacitor properties of VS_2.

Herein, we successfully doped Mo atoms into the VS_2 lattice by one-pot hydrothermal method. The material characterization results indicate that the incorporation of Mo can increase the specific surface area and interlayer spacing of VS_2. As a result, the Mo-doped VS_2 shows an excellent supercapacitor performance. The Mo-doped VS_2 has a specific capacity of 170 F g^{-1} at 0.5 A g^{-1} for a three-electrode system. Furthermore, the symmetric supercapacitor made by the Mo-doped VS_2 presented superior energy density. The incorporation of Mo in VS_2 could greatly increase the electrochemically active surface area and electrical conductivity, resulting in a dramatically enhanced activity for double-layer supercapacitors. The results exemplify that Mo-doped VS_2 can be a suitable material as a high-efficiency electrode for potential supercapacitor applications.

2. Results and Discussion

The crystallographic structures of the pristine VS_2 and Mo-doped VS_2 were determined via Raman and X-ray diffraction (XRD) spectra (Figure 1). The XRD patterns suggest that all the diffraction peaks can be matched with hexagonal VS_2 (PDF# 89-1640) without obvious contaminants [18,19], indicating the single phase of Mo-doped VS_2 (Figure 1a, Table S1). A shift to lower angles after Mo doping was observed in the enlarged view of the (001) peaks of the range of 2θ = 10.0~20.0°. Such a peak shift suggests an increase in (001) lattice spacing due to the Mo dopant [26,27]. In the meantime, the increased (001) peak width of the Mo-doped VS_2 may suggest grain refinement after Mo doping [28,29]. The Raman spectra exhibit a series of bands between 100 and 1200 cm^{-1} (Figure 1c) for the Mo-doped VS_2 and pristine VS_2, which are consistent with those of VS_2 [25,26]. The E_{1g} mode at 282.1 cm^{-1} originates from in-plane sulfur atom vibrations opposing the vanadium center, while the A_{1g} peak at 403.5 cm^{-1} linked to out-of-plane sulfur displacements along the c-axis [30–32]. In addition, the Mo-doped VS_2 has a new band at 300.5 cm^{-1}, which may be caused by the lattice mismatch induced by Mo doping [33].

The X-ray photoelectron spectroscopy (XPS) analyzed the surface chemical states and elemental composition of the Mo-doped VS_2 and pristine VS_2. In comparison to the pristine VS_2, the XPS survey spectra of the Mo-doped VS_2 suggest two additional weak Mo 3p peaks (Figure 2a), confirming the presence of the Mo element. The V^{4+} and V^{2+} states are represented by the doublet peaks at 523.5, 516.0, and 521.3, 513.8 eV in the V 2p spectra for the Mo-doped VS_2 and pristine VS_2 (Figure 2b) [34–36]. The S 2p spectrum of the pristine VS_2 exhibits two doublet peaks at 162.3, 161.2, and 163.9, 162.7 eV (Figure 2c), which are indicative of S^{2-} and metal-sulfur species [35,36]. Interestingly, compared to the pristine VS_2, the binding energy of S^{2-} 2p peaks has a positive shift of roughly 0.3 eV, indicating the successful doping of Mo atoms [37]. The Mo 3d spectrum of the Mo-doped VS_2 exhibits two deconvoluted doublets at 228.8/232.0 eV and 229.9/233.2 eV (Figure 2d), which corroborate the Mo^{4+}, Mo^{5+} species following Mo doping [38]. The energy dispersive X-ray (EDX) result shows that the Mo doping concentration estimated from the atomic ratio of Mo/(V+Mo) is approximately 7.4% for the Mo-doped VS_2 (Figure S1), which is slightly lower than the ratio in precursors, and it suggests that only a fraction of the Mo atoms in precursors were successfully incorporated into the VS_2 [39]. Combined with the XPS, XRD,

and Raman patterns, the EDX results verify the successful doping of the Mo atoms into the VS_2 matrix.

The morphologies and microstructures were examined using a field-emission scanning electron microscope (FESEM) (Figure 3) and transmission electron microscope (TEM) (Figure 4a–f) for the Mo-doped VS_2 and pristine VS_2. Both the pristine VS_2 and Mo-doped VS_2 exhibit hierarchical nanosheet structure and flower-like morphologies, and the sizes of microflowers decrease significantly from 6~9 μm for the pristine VS_2 to 1~3 μm for the Mo-doped VS_2 (Figures 3 and 4a,d). The decrease in microflower size may suggest an increased surface area, which may contribute to more exposed active sites and result in improved supercapacitor performances [39,40]. The Mo dopant's suppression of VS_2 grain formation may be the cause of the decreased size of the microflower [41]. The interlayer spacing of the (001) plane was measured to be 0.584 nm for the Mo-doped VS_2 (Figure 4e), representing a 1.2% lattice expansion compared to the pristine VS_2 (0.577 nm) (Figure 4b). A larger interlayer spacing will bring faster ion kinetics and greater ion-accessible surface, which can improve the supercapacitor properties [39,40]. A periodic lattice fringe pattern is suggested by the HRTEM image projected along the c-axis, and the corresponding selected area electron diffraction (SAED) patterns support the hexagonal structure (Figure 4c,f) [42]. The EDX result confirms the uniform distribution of Mo, V, and S elements throughout the examination area in the Mo-doped VS_2 (Figure 4g), indicating the uniform compositions of the Mo-doped VS_2.

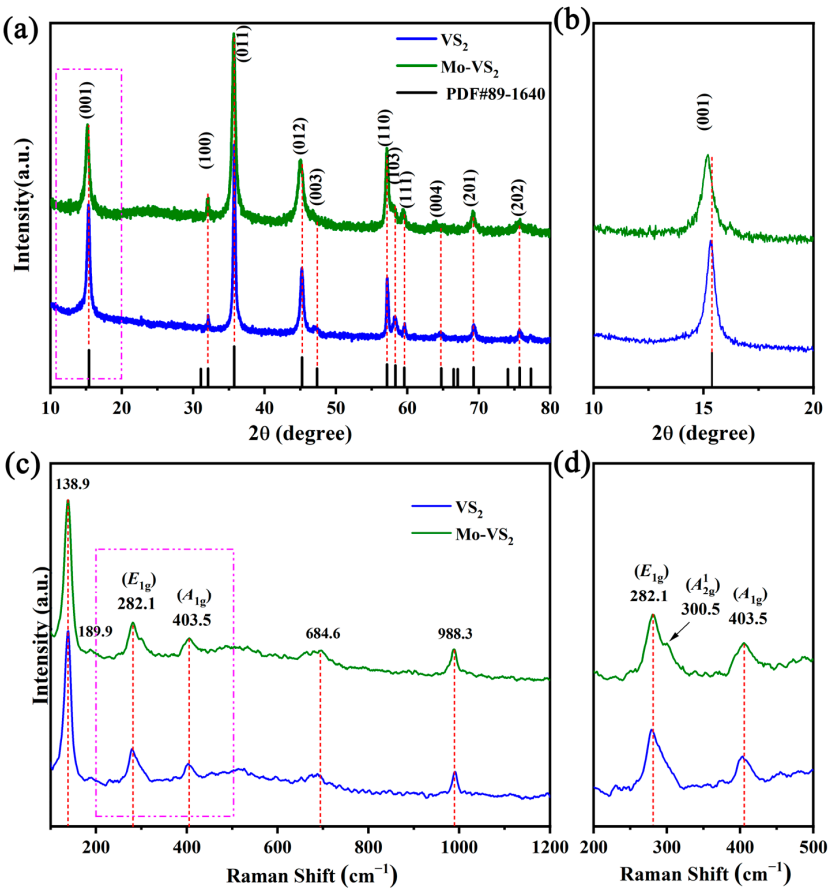


Figure 1. (**a**) XRD patterns and (**c**) Raman spectra of the Mo-doped VS_2 and pristine VS_2. The (**b**) is the enlarged region of 2θ = 10.0~20.0°, and the (**d**) is the enlarged region of 200~500 cm^{-1}. The red dotted line indicates the comparison of peak positions between VS_2 and Mo-doped VS_2.

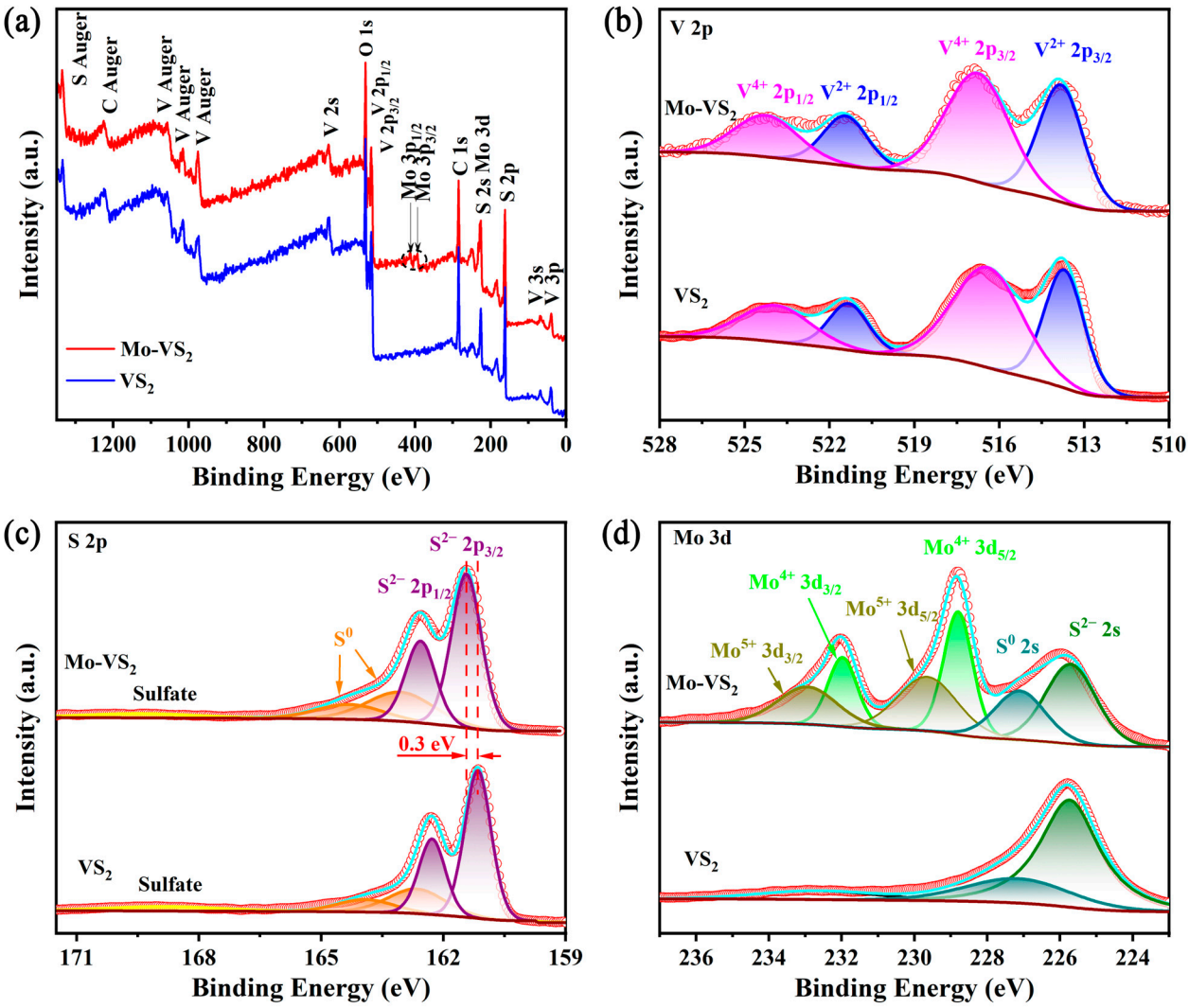


Figure 2. (**a**) XPS survey spectra, (**b**) V 2p, (**c**) S 2p, and (**d**) Mo 3d of high-resolution spectra for the pristine VS_2 and Mo-doped VS_2.

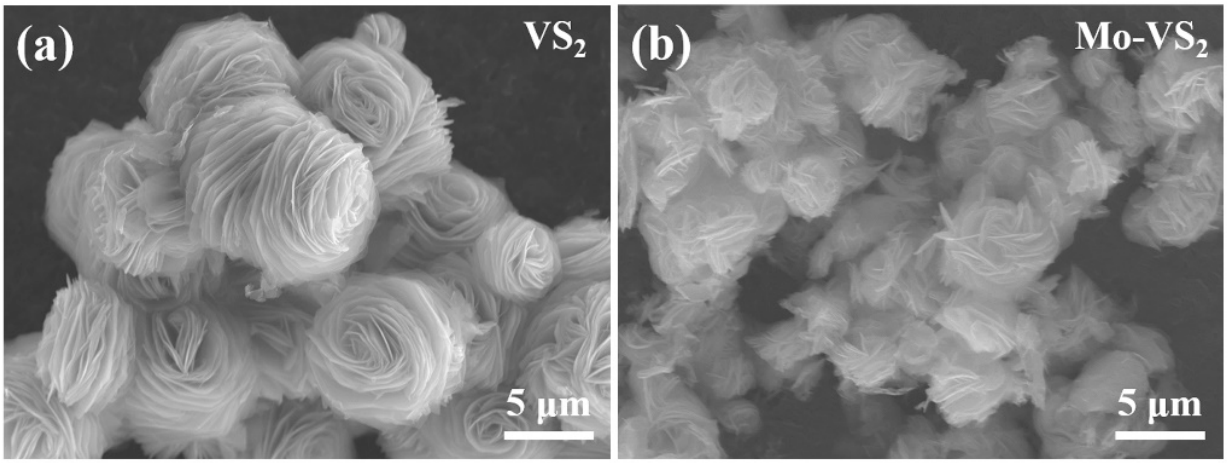


Figure 3. FESEM images for the (**a**) pristine VS_2 and (**b**) Mo-doped VS_2.

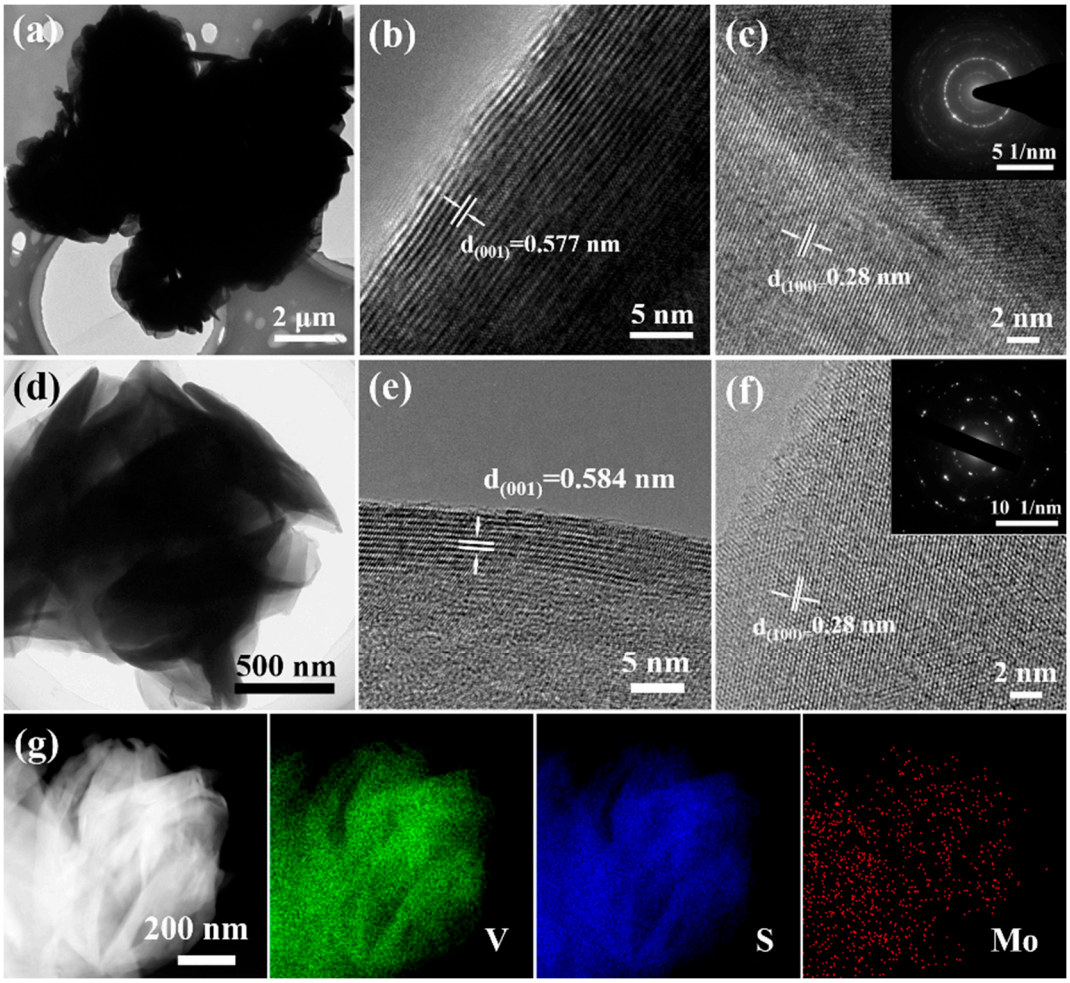


Figure 4. (**a**) Low-magnification and (**b**,**c**) high-magnification TEM images of the pristine VS_2; the inset of (**c**) is the matching SAED pattern. (**d**) Low-magnification and (**e**,**f**) high-magnification TEM images, and (**g**) elemental mapping of the Mo-doped VS_2; the inset of (**f**) is the corresponding SAED pattern.

Figure 5 displays the nitrogen adsorption–desorption isotherm and pore-size distribution curves for the Mo-doped VS_2 and pristine VS_2. The mesoporous nature and slit-like pores are indicated by the type IV isotherms for the Mo-doped VS_2 and pristine VS_2 with an H3 hysteresis loop (Figure 5a) [43,44]. The Brunauer–Emmette–Teller (BET) specific surface area of the Mo-doped VS_2 was determined to be 10.77 m^2 g^{-1} using the nitrogen adsorption–desorption isotherms, substantially greater than the pristine VS_2 (5.72 m^2 g^{-1}). The pore sizes of the two samples are mainly concentrated in 1~10 nm, and the pore volume of the Mo-doped VS_2 is significantly greater compared to the pristine VS_2 (Figure 5b). The enhanced pore architecture and expanded surface area of Mo-doped VS_2 potentially optimize charge storage capacity through increased active site accessibility [45]. Therefore, the Mo-doped VS_2 is anticipated to demonstrate a notable improvement in supercapacitor performance compared to pristine VS_2.

The electrochemical performances of the Mo-doped VS_2 and pristine VS_2 electrodes were evaluated using the three-electrode system in 1.0 M Na_2SO_4. Figure 6a for the Mo-doped VS_2 and Figure S2a for the pristine VS_2 displays the cyclic voltammetry (CV) curves at various scan rates. The typical electric double-layer capacitance behavior is shown through the rectangular-like shapes of all the CV curves, which lack noticeable redox peaks [46,47]. Figure 6b compares the CV curves of the pristine VS_2 and Mo-doped VS_2 at a scan rate of 20 mV s^{-1}. Compared to the pristine VS_2, the integrated area of the

CV curve for the Mo-doped VS_2 is greater, indicating a higher capacitance. According to Equation (S1), the specific capacitances of the Mo-doped VS_2 and pristine VS_2 versus scan rates were computed, as displayed in Figure 6c. The Mo-doped VS_2 exhibits superior rate performance compared to the pristine VS_2, delivering 301.6 F g^{-1} at 5 mV s^{-1} with 46.9% capacity preservation (141.3 F g^{-1}) at 100 mV s^{-1}. The galvanostatic charge–discharge (GCD) curves at different current densities are displayed in Figure 6d for the Mo-doped VS2 and Figure S2b for the pristine VS_2. All the GCD curves are triangular and linearly symmetrical, demonstrating excellent supercapacitor performance and high coulombic efficiency [46,47]. Figure 6e compares the GCD curves of the pristine VS_2 and Mo-doped VS_2 at 1 A g^{-1}. As expected, a much longer charging–discharging time appeared under the GCD curve for the Mo-doped VS_2 (Figure 6e), which further indicates its higher capacitance than the pristine VS_2 [46], in conformity with the CV results. Figure 6f displays the specific capacitance of the Mo-doped VS_2 and pristine VS_2 versus current densities, calculated by Equation (S2). The Mo-doped VS_2 demonstrates good rate capability with the specific capacitance of 170 F g^{-1} at 0.5 A g^{-1} and 96.4 F g^{-1} at 5 A g^{-1}.

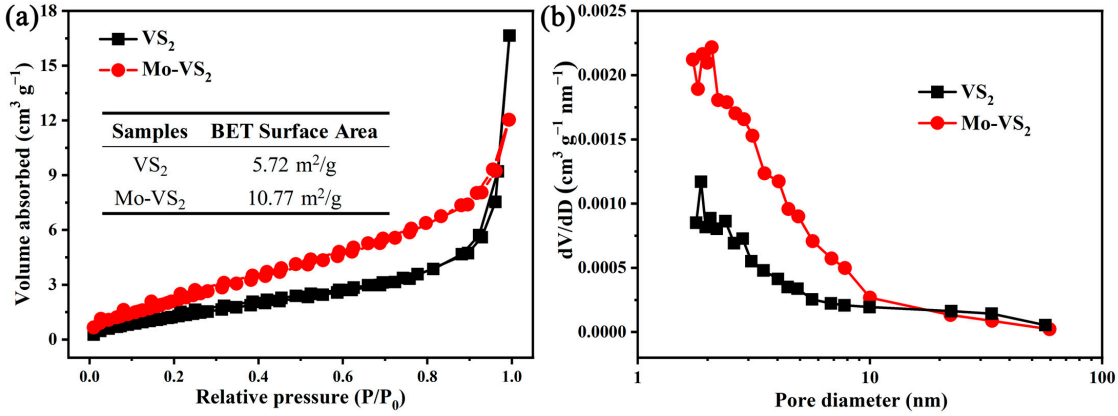


Figure 5. (**a**) Nitrogen adsorption–desorption isotherms and (**b**) pore-size distribution curves of the Mo-doped VS_2 and pristine VS_2.

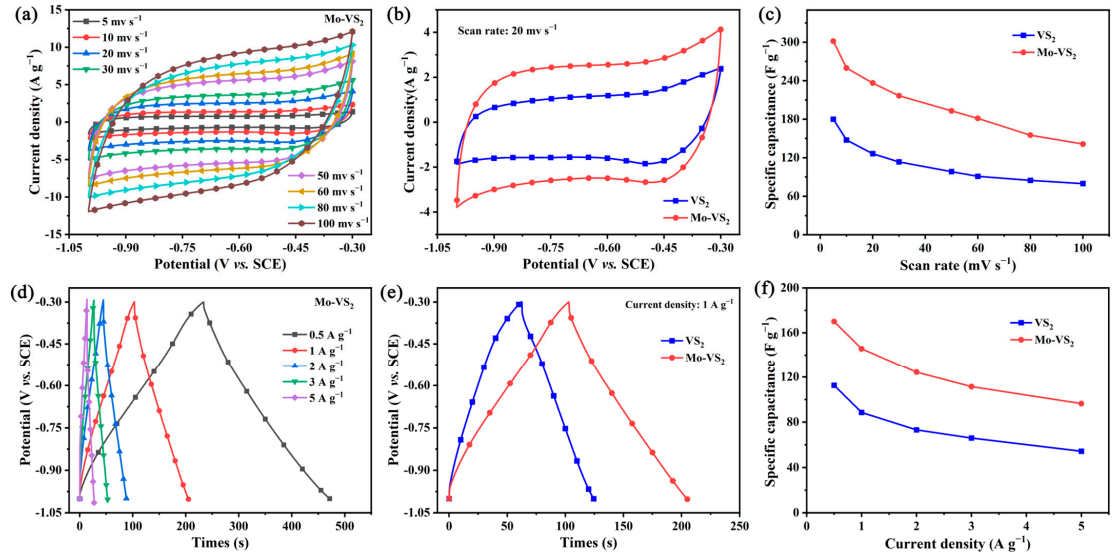


Figure 6. Electrochemical performance of the Mo-doped VS_2- and pristine VS_2-based three-electrode systems: (**a**) CV curves of the Mo-doped VS_2 at various scan rates; (**b**) comparison of CV curves at 20 mV s^{-1}; (**c**) specific capacitance versus scan rate; (**d**) GCD curves of the Mo-doped VS_2 at various current densities; (**e**) comparison of GCD curves at 1 A g^{-1}; (**f**) Specific capacitance versus current density.

Meanwhile, the EIS measurement was performed to further investigate the ion/electron transport properties. Figure 7 shows the Nyquist plots and cycle stability curves for the pristine VS_2 and Mo-doped VS_2 in the three-electrode system. In Figure 7a, the equivalent series resistances (R_s) for the pristine VS_2 and Mo-doped VS_2 are calculated to be 1.0 and 2.3 Ω, respectively. The Mo-doped VS_2 has a decreased charge transfer resistance (R_{ct}) at 3 Ω than the pristine VS_2 (4.2 Ω). Furthermore, in the low-frequency region, the Mo-doped VS_2 shows more nearly vertical than pristine VS_2, indicating that it has a lower Warburg resistance coefficient (0.094 Ω $s^{-0.5}/cm^2$) than pristine VS_2 (0.165 Ω $s^{-0.5}/cm^2$). This implies that the Mo-doped VS_2 has a faster rate of electrons and electrolyte ion diffusion at the electrode/electrolyte interface than the pristine VS_2 [47,48]. The cycling stability of the Mo-doped VS_2 and pristine VS_2 were assessed using 3000 GCD cycles at 2 A g^{-1} (Figure 7b). The Mo-doped VS_2 has a greater specific capacitance than the pristine VS_2 over 2000 cycles. After 2000 cycles, the capacitance of Mo-doped VS_2 is maintained at 99.7 F g^{-1} and the capacity preservation reaches 80.3%. The capacity enhancement is presumably ascribed to the incorporation of Mo, which elicited larger interlayer spacing, good conductivity, and higher specific surface area, thereby forming more accessible active sites and faster electron and electrolyte ion diffusion kinetics [20–22].

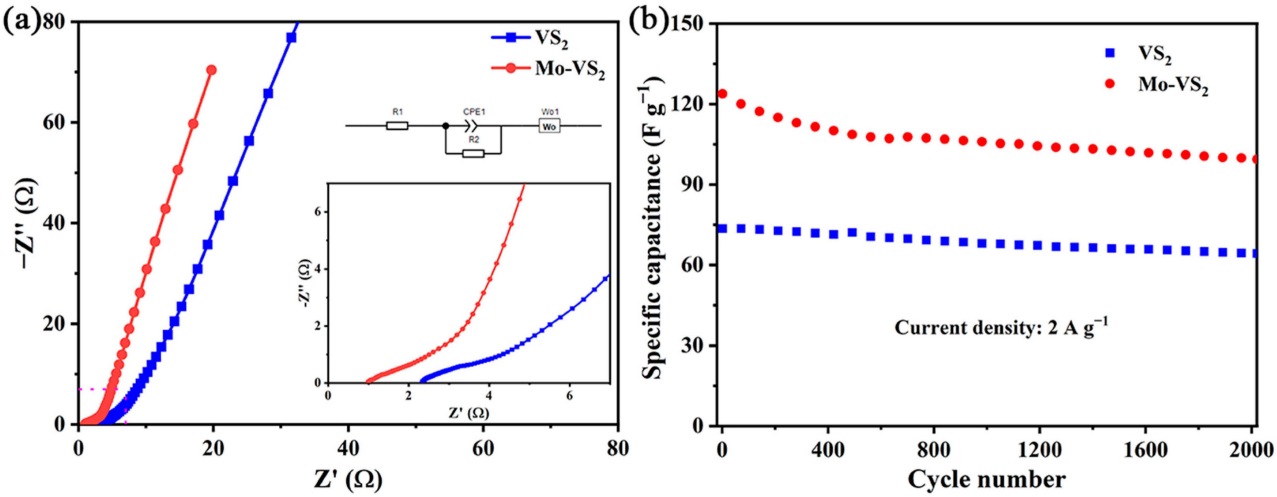


Figure 7. Electrochemical performance of the Mo-doped VS_2 and pristine VS_2-based three-electrode systems: (**a**) Nyquist plots at open circuit voltage; (**b**) cycle stability of the Mo-doped VS_2 and pristine VS_2 for 2000 cycles at 2 A g^{-1}.

Moreover, we assembled the symmetric supercapacitor using the Mo-doped VS_2 electrode to evaluate the practical application in 1 M Na_2SO_4. Figure 8a for the Mo-doped VS_2 and Figure S3 for the pristine VS_2 show the CV curves at various scan rates. The typical double-layer capacitance behavior is shown through the rectangular-like shapes of all the CV curves, which lack noticeable redox peaks [49]. Figure S4 compares the CV curves at 20 mV s^{-1} for the pristine VS_2 and Mo-doped VS_2, where the Mo-doped VS_2 exhibits a larger CV-integrated area than the pristine VS_2, suggesting a high capacitance [50]. As displayed in Figure S4, Equation (S3) was utilized to evaluate the specific capacitance of the button-type symmetric supercapacitor for the Mo-doped VS_2 and pristine VS_2 at various scan rates. The Mo-doped VS_2 reveals a superior capacitive performance of 389.5 F g^{-1} at 5 mV s^{-1} and 143.0 F g^{-1} at 100 mV s^{-1} (Figure S5). The GCD curves show the triangular shapes and linear symmetry for the Mo-doped VS_2 (Figure 8b) and pristine VS_2 (Figure S6), and they again display outstanding capacitive behavior [49]. Figure S7 compares the GCD curves at 1 A g^{-1} for the pristine VS_2 and Mo-doped VS_2, where the Mo-doped VS_2 presents a longer charge–discharge time compared to the pristine VS_2,

suggesting its good capacitance [50]. The specific capacitance of the Mo-doped VS_2 achieves a high specific capacitance of 245.7 F g^{-1} at 0.25 A g^{-1} and 85.7 F g^{-1} at 3 A g^{-1} (Figure 8c), indicating its good rate performance. These indicate that the Mo-doped VS_2 has a greater capacitance than the pristine VS_2. Furthermore, the stability of the pristine VS_2 and Mo-doped VS_2 was assessed using 1000 GCD cycles at 2 A g^{-1} (Figure 8d). The Mo-doped VS_2 has a greater specific capacitance than the pristine VS_2 over 2000 cycles. After 1000 cycles, the capacitance of Mo-doped VS_2 is maintained at 99.7 F g^{-1} and the capacity preservation reaches 73.3% (Figure 8d). The equivalent series resistances (R_s) of the Mo-doped VS_2 and pristine VS_2 are calculated to be 1.6 and 2.6 Ω, respectively (Figure S8), and the Mo-doped VS_2 has a decreased charge transfer resistance (R_{ct}) of 2.8 Ω than pristine VS_2 (9.2 Ω). What is more, in the low-frequency region, the Mo-doped VS_2 shows more nearly vertical than that of the pristine VS_2, indicating a lower Warburg resistance. This implies that the Mo-doped VS_2 has a faster rate of electrons and electrolyte ion diffusion at the electrode/electrolyte interface than the pristine VS_2 [47,48]. The Ragone figure (Figure 8e) illustrates the correlation between the power density and energy density of the Mo-doped VS_2 and pristine VS_2. At power densities of 87.5 and 1050 W kg^{-1}, the corresponding energy densities for the Mo-doped VS_2 were 4.19 and 1.46 Wh kg^{-1}, respectively. The energy density of Mo-doped VS_2 surpassed some MoS_2-based symmetric supercapacitors, such as MoS_2/PPY [51], MoS_2/TiO_2/Ti [52], and 1T/2H MoS_2 [53] (Table S2). The practical viability assessment of the Mo-doped VS_2 based on a button-type symmetric supercapacitor demonstrated successful operation in real-world scenarios, evidenced by powering a commercial green LED (2.1 V threshold) through three serially connected coin-cell devices (Figure 8f). These findings imply the potential of the Mo-doped VS_2 as the candidate alternative electrode material for emerging energy storage systems.

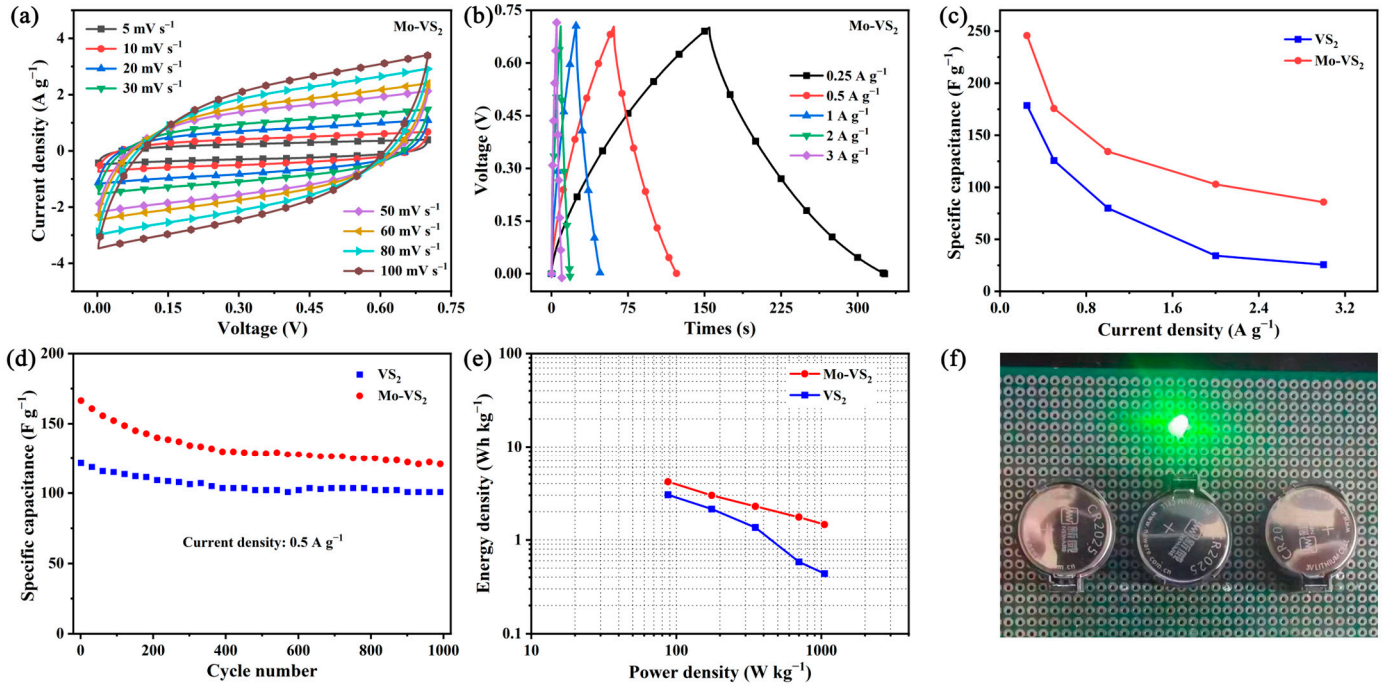


Figure 8. Electrochemical characterization of the Mo-doped VS_2 and pristine VS_2 based on the two-electrode symmetric supercapacitor: (**a**) CV curves of the Mo-doped VS_2 at various scan rates; (**b**) GCD curves of the Mo-doped VS_2 at various current densities; (**c**) comparison of specific capacitance for the Mo-doped VS_2 and pristine VS_2; (**d**) stability of the Mo-doped VS_2 and pristine VS_2 for 1000 cycles at 0.5 A g^{-1}; (**e**) Ragone curve of energy density versus power density; (**f**) the digital image of a green-LED bulb powered by the symmetric supercapacitor.

3. Experimental

3.1. Synthesis of the Mo-Doped VS_2 and Pristine VS_2 Microflowers

The preparation of Mo-doped VS_2 microflowers involved the following steps: Initially, 1.8 mmol ammonium vanadate (NH_4VO_3, Aladdin, 99.95%, Shanghai, China) and 0.0286 mmol ammonium molybdate tetrahydrate ($(NH_4)_6Mo_7O_{24}{\cdot}4H_2O$, Aladdin, 99.9%, Shanghai, China) were mixed with 38 mL deionized water and 2 mL ammonia ($NH_3{\cdot}H_2O$, Aladdin, 25~28%, Shanghhai, China) to form a transparent solution. Subsequently, 20 mmol thioacetamide (CH_3CSNH_2, Sigma-Aldrich, 99%, Shanghai, China) was introduced into the mixture and magnetically stirred for 10 min, resulting in a pale-yellow liquid phase. The precursor solution was hydrothermally processed in a 50 mL Teflon reactor at 160 °C for 24 h. Following natural cooling to room temperature, the resultant black precipitate underwent sequential purification—deionized water/ethanol washing cycles followed by 30 h lyophilization to yield the target composite. For reference, the pristine VS_2 was fabricated using an identical protocol excluding the molybdenum precursor.

3.2. Materials Characterization

Phase identification and crystallographic analysis were performed via XRD (Ultima IV, Rigaku, Tokyo, Japan) with Cu Kα1 radiation (λ = 0.15418 nm), complemented by Raman spectroscopy (Invia RM200, Renishaw, Gloucestershire, UK) employing a 532 nm excitation laser. Chemical state characterization was carried out through XPS (ESCALAB 250Xi, ThermoFisher VG Scientific, Waltham, MA, USA) with a monochromatic Al Kα X-ray source. The morphological and compositional features were examined by FESEM (SU5000, Hitachi, Tokyo, Japan) equipped with EDX detector (Inca 250, Oxford, UK), alongside spherical aberration-corrected S/TEM (Titan G2 60-300, FEI, Hillsboro, OR, USA). Specific surface area quantification was achieved by the BET analysis of nitrogen adsorption–desorption isotherms recorded on a surface area and porosity analyzer (TriStar II 3020, Micromeritics, Norcross, GA, USA).

3.3. Electrochemical Measurements

Electrochemical evaluations were carried out at ambient temperature using an electrochemical workstation (CHI660E, CH Instruments, Inc., Shanghai, China). Initially, the intrinsic performance of te Mo-doped VS_2 and pristine VS_2 was assessed in a three-electrode configuration. To explore practical applicability, a symmetric two-electrode supercapacitor cell was subsequently fabricated with these materials. The electrochemistry characterization methods involved CV, GCD, EIS, and cyclic stability. Detailed protocols for electrode fabrication, symmetric two-electrode supercapacitor assembly, and measurement parameters are provided in the Supplementary Materials.

4. Conclusions

In summary, the Mo-doped VS_2 microflower has been fabricated through a one-pot hydrothermal method. The structural analyses reveal that the Mo-doped VS_2 possesses a specific surface area of 10.77 $m^2\ g^{-1}$ and interlayer spacing of 0.584 nm, which are much higher than those of the pristine VS_2 (5.72 $m^2\ g^{-1}$ and 0.577 nm). The electrochemical evaluations demonstrate that the Mo-doped VS_2 has a specific capacitance of 389.5 F g^{-1} at 5 mV s^{-1} and 145.7 F g^{-1} at 1 A g^{-1}. Furthermore, the symmetric supercapacitor based on the Mo-doped VS_2 exhibits good stability and ideal rate capability. It provides a high specific capacitance of 245.7 F g^{-1} at 0.25 A g^{-1}, a maximum energy density of 4.19 h kg^{-1}, and good stability (73.3% capacity preservation after 1000 cycles at 0.5 A g^{-1}). Importantly, practical viability was further confirmed through the successful powering of commercial LEDs using button-type symmetric supercapacitors. The capacity enhancement is probably

ascribed to the increased active surface area, expanded interlayer spacing, and optimized electronic conductivity Mo doping. The findings collectively position Mo-doped VS_2 as a promising candidate for emerging energy storage systems.

Supplementary Materials: The following supporting information can be downloaded at https://www.mdpi.com/article/10.3390/inorganics13060199/s1, Figure S1: EDX spectrum of the Mo-doped VS_2 microflowers; Figure S2: Electrochemical performance of the Mo-doped VS_2 and pristine VS_2-based three-electrode system: (a) CV curves at different scan rates; (b) GCD curves at different current densities; Figure S3: CV curves at different current densities for pristine VS_2 based on the symmetric supercapacitor; Figure S4: Comparison of CV curves for the Mo-doped VS_2 and pristine VS_2 based on the symmetric supercapacitor at 10 mV s^{-1}; Figure S5: Specific capacitance of the symmetric supercapacitor for the Mo-doped VS_2 and pristine VS_2 at various scan rates; Figure S6: GCD curves of the pristine VS_2 at various current densities based on the symmetric supercapacitor.; Figure S7: Comparison of GCD curves for the Mo-doped VS_2 and pristine VS_2 based on the symmetric supercapacitor at 1 A g^{-1}; Figure S8: Nyquist plots of symmetric supercapacitor based on the Mo-doped VS_2 and pristine VS_2 electrode at open circuit voltage. Table S1: Comparison of crystallographic parameters for pristine VS_2 and Mo-doped VS_2; Table S2: Comparison of electrochemical performance with other reports. References [54–57] are cited in the Supplementary Materials.

Author Contributions: Conceptualization, J.W. and W.H.; methodology, J.W. and W.H.; validation, J.W. and W.H.; formal analysis, J.W. and W.H.; investigation, J.W., L.X., Z.X. and W.H.; data curation, J.W.; resources, W.H. and X.Z.; writing—original draft preparation, J.W. and W.H.; writing—review and editing, J.W. and W.H.; funding acquisition, X.Z. and W.H. All authors have read and agreed to the published version of the manuscript.

Funding: This study was supported by National Key R&D Program of China (2021YFB4000800), National Natural Science Foundation of China (12302204), Hefei General Machinery Research Institute Co., LTD. (20213 ZK 2021010483), the Project of Hunan Provincial Department of Education (24C0035), and Guangdong Basic and Applied Basic Research Foundation (2022A1515110091).

Institutional Review Board Statement: Not applicable.

Informed Consent Statement: Not applicable.

Data Availability Statement: Dataset available upon request from the authors.

Conflicts of Interest: Hefei General Machinery Research Institute Co., LTD. provided funding assistance (20213 ZK 2021010483) for this research. The company had no role in design of the study; in the collection, analyses or interpretation of data; in the writing of the manuscript; or in the decision to publish the results.

References

1. Simon, P.; Gogotsi, Y.; Dunn, B. Where do batteries end and supercapacitors begin? *Science* **2014**, *343*, 1210–1211. [CrossRef] [PubMed]
2. Simon, P.; Gogotsi, Y. Perspectives for electrochemical capacitors and related devices. *Nat. Mater.* **2020**, *19*, 1151–1163. [CrossRef] [PubMed]
3. Liu, C.; Yu, Z.; Neff, D.; Zhamu, A.; Jang, B.Z. Graphene-based supercapacitor with an ultrahigh energy density. *Nano Lett.* **2010**, *10*, 4863–4868. [CrossRef] [PubMed]
4. Choudhary, N.; Li, C.; Moore, J.; Nagaiah, N.; Zhai, L.; Jung, Y.; Thomas, J. Asymmetric supercapacitor electrodes and devices. *Adv. Mater.* **2017**, *29*, 1605336. [CrossRef]
5. Nallapristineddy, J.; Nallapristineddy, R.R.; Thomas, S.A.; Arla, S.K.; Cherusseri, J.; Prabu, S.; Pallavolu, M.R.; Joo, S.W. Hierarchical nickel molybdenum sulfide whisker nanoneedles: Binder-free in situ grown electrodes designed for enhanced supercapattery performance. *J. Energy Storage* **2025**, *123*, 116864.
6. Panghal, A.; Sahoo, D.; Deepak, D.; Deshmukh, S.; Kaviraj, B.; Roy, S.S. Single-step synthesis of Ni-doped MoS_2 nanostructures for symmetrical supercapacitor devices. *ACS Appl. Nano Mater.* **2024**, *7*, 5358–5371. [CrossRef]
7. De, A.A.; Singh, S.; Lahiri, I. WS_2@PPy heterostructured high performance supercapacitor self-powered by PVDF piezoelectric separator. *J. Alloys Compd.* **2023**, *939*, 168713.

8. Yogesh, G.K.; Nandi, D.; Yeetsorn, R.; Wanchan, W.; Devi, C.; Singh, R.P.; Vasistha, A.; Kumar, M.; Koinkar, P.; Yadav, K. A machine learning approach for estimating supercapacitor performance of graphene oxide nano-ring based electrode materials. *Energy Adv.* **2025**, *4*, 119–139. [CrossRef]
9. Šedajová, V.; Nandi, D.; Langer, P.; Lo, R.; Hobza, P.; Plachá, D.; Bakandritsos, A.; Zbořil, R. Direct upcycling of highly efficient sorbents for emerging organic contaminants into high energy content supercapacitors. *J. Colloid. Interface Sci.* **2025**, *692*, 137481. [CrossRef]
10. Liu, Y.Y.; Xu, L.; Guo, X.T.; Lv, T.T.; Pang, H. Vanadium sulfide based materials: Synthesis, energy storage and conversion. *J. Mater. Chem. A* **2020**, *8*, 20781–20802. [CrossRef]
11. Koudahi, M.F.; Frąckowiak, E. Fast response supercapacitor based on carbon-VS_2 electrodes with a wide operating voltage range. *Energy Storage Mater.* **2022**, *49*, 255–267. [CrossRef]
12. Wang, H.; You, L.; Guan, Y.; Wang, H.; Ma, X.; Wang, D.; Wu, J.; Zhu, Y.; Lin, J.; Liu, J. Rational fabrication of flower-like VS_2-decorated Ti_3C_2 MXene heterojunction nanocomposites for supercapacitance performances. *Colloids Surf. A* **2021**, *629*, 127381. [CrossRef]
13. Hu, B.; Zhang, Y.; Zhang, J.; Liu, J.; Lei, M.; Zhao, C.; Lu, Q.; Wang, H.; Du, F.; Zhang, S. Solar light-driven photoelectrocatalytic and photocatalytic applications based on flower-like NV-g-C_3N_5@VS_2 heterojunctions. *New J. Chem.* **2023**, *47*, 10973–10983. [CrossRef]
14. He, W.; Zheng, X.; Peng, J.; Zhang, Q.; Pei, D.; Yan, X. One-step solid-phase synthesis of binder-free molybdenum disulfide/carbon fibers paper anode for high-performance lithium-ion batteries. *J. Alloys Compd.* **2018**, *768*, 33–41. [CrossRef]
15. Pandit, B.; Karade, S.S.; Sankapal, B.R. Hexagonal VS_2 anchored MWCNTs: First approach to design flexible solid-state symmetric supercapacitor device. *ACS Appl. Mater. Interfaces* **2017**, *9*, 44880–44891. [CrossRef]
16. Zhang, Q.; He, W.; Wang, Y.; Pei, D.; Zheng, X. Sonication-assisted synthesis of molybdenum disulfide aerogel for the electrode materials of supercapacitors. *Nano* **2019**, *14*, 1950055. [CrossRef]
17. Pandit, B.; Bommineedi, L.K.; Sankapal, B.R. Electrochemical engineering approach of high performance solid-state flexible supercapacitor device based on chemically synthesized VS_2 nanoregime structure. *J. Energy Chem.* **2019**, *31*, 79–88. [CrossRef]
18. Wang, J.; Dong, Y.; Zheng, X.; Long, B.; Ling, H.; Xie, L.; Xiang, Z.; He, W. P non-metal doping induced surface charge redistribution of VS_2 for strengthening hydrogen evolution activity. *Appl. Surf. Sci.* **2025**, *694*, 162834. [CrossRef]
19. Yuan, Y.; Xu, Q.; Yang, G.; Lin, J. Study of super capacitive energy storage properties of VS_2 electrode materials. *Appl. Surf. Sci.* **2025**, *688*, 162453. [CrossRef]
20. Isacfranklin, M.; Princy, L.E.M.; Rathinam, Y.; Kungumadevi, L.; Ravi, G.; Al-Sehemi, A.G.; Velauthapillai, D. Rare earth-doped MoS_2 for supercapacitor application. *Energy Fuels* **2022**, *36*, 6476–6482. [CrossRef]
21. Saseendran, S.B.; Ashok, A.; Asha, A.S. Flexible and binder-free supercapacitor electrode with high mass loading using transition metal doped MoS_2 nanostructures. *J. Alloys Compd.* **2023**, *968*, 172131. [CrossRef]
22. Robertson, B.; Sapna, R.; Hareesh, K. A comprehensive review on $MoSe_2$ nanostructures with an overview of machine learning techniques for supercapacitor applications. *RSC Adv.* **2024**, *14*, 37644–37675.
23. Masanta, S.; Nayak, C.; Maitra, S.; Rudra, S.; Chowdhury, D.; Raha, S.; Pradhan, M.; Satpati, B.; Pal, P.; Singha, A. Engineering multifunctionality in $MoSe_2$ nanostructures via strategic Mn doping for electrochemical energy storage and photosensing. *ACS Appl. Nano Mater.* **2023**, *6*, 5479–5492. [CrossRef]
24. Qu, Y.; Pan, H.; Kwok, C.T.; Wang, Z. Effect of doping on hydrogen evolution reaction of vanadium disulfide monolayer. *Nanoscale Res. Lett.* **2015**, *10*, 480. [CrossRef]
25. He, W.; Zheng, X.; Peng, J.; Dong, H.; Wang, J.; Zhao, W. Mo-dopant-strengthened basal-plane activity in VS_2 for accelerating hydrogen evolution reaction. *Chem. Eng. J.* **2020**, *396*, 125227. [CrossRef]
26. Feng, J.; Wu, C.; Peng, L.; Lin, C.; Hu, S.; Yang, J.; Xie, Y. Metallic few-layered VS_2 ultrathin nanosheets: High two-dimensional conductivity for in-plane supercapacitors. *J. Am. Chem. Soc.* **2011**, *133*, 17832–17838. [CrossRef]
27. Xu, X.; Ge, Y.; Wang, M.; Zhang, Z.; Dong, P.; Baines, R.; Ye, M.; Shen, J. Cobalt-doped $FeSe_2$-RGO as highly active and stable electrocatalysts for hydrogen evolution reactions. ACS Appl. *Mater. Interfaces* **2016**, *8*, 18036–18042. [CrossRef]
28. Ding, S.; Li, Z.; Dai, X.; Li, Z.; Dai, X.; Sun, C.; Meng, A. Mo-doped VS_4 with interlayer-expanded and engineering sulfur vacancies as cathode for advanced magnesium storage. *Chem. Eng. J.* **2021**, *417*, 129328. [CrossRef]
29. Yu, L.; Zhao, S.; Yuan, Y.; Wei, G.; Zhao, J. Mo-doped induced amorphous phase and sulfur vacancy healing in VS_4 for enhancing the storage of lithium ions. *J. Mater. Chem. A* **2021**, *9*, 1100–1109. [CrossRef]
30. He, P.; Yan, M.; Zhang, G.; Sun, R.; Chen, L.; An, Q.; Mai, L. Layered VS_2 nanosheet-based aqueous Zn ion battery cathode. *Adv. Energy. Mater.* **2017**, *7*, 1601920. [CrossRef]
31. Wu, L.; Sun, R.; Xiong, F.; Pei, C.; Han, K.; Peng, C.; Fan, Y.; Yang, W.; An, Q.; Mai, L. A rechargeable aluminum-ion battery based on a VS_2 nanosheet cathode. *Phys. Chem. Chem. Phys.* **2018**, *20*, 22563–22568. [CrossRef]
32. Sun, R.; Wei, Q.; Sheng, J.; Shi, C.; An, Q.; Liu, S.; Mai, L. Novel layer-by-layer stacked VS_2 nanosheets with intercalation pseudocapacitance for high-rate sodium ion charge storage. *Nano Energy* **2017**, *35*, 396–404. [CrossRef]

33. Sourisseau, C.; Cavagnat, R.; Fouassier, M.; Tirado, J.L.; Morales, J. Raman study and lattice dynamics calculations of misfit layered compounds: $(PbS)_{1.18}TiS_2$ and $(PbS)_{1.12}VS_2$. *J. Mol. Struct.* **1995**, *348*, 107–110. [CrossRef]
34. Zhang, J.; Zhang, C.; Wang, Z.; Zhu, J.; Wen, Z.; Zhao, X.; Zhang, X.; Xu, J.; Lu, Z. Synergistic interlayer and defect engineering in VS_2 nanosheets toward efficient electrocatalytic hydrogen evolution reaction. *Small* **2018**, *14*, 1703098. [CrossRef] [PubMed]
35. Chia, X.; Ambrosi, A.; Lazar, P.; Sofer, Z.; Pumera, M. Electrocatalysis of layered Group 5 metallic transition metal dichalcogenides (MX_2, M = V, Nb, and Ta; X = S, Se, and Te). *J. Mater. Chem. A* **2016**, *4*, 14241–14253. [CrossRef]
36. Xue, X.; Chen, R.; Yan, C.; Zhao, P.; Hu, Y.; Kong, W.; Lin, H.; Wang, L.; Jin, Z. One-step synthesis of 2-ethylhexylamine pillared vanadium disulfide nanoflowers with ultralarge interlayer spacing for high-performance magnesium storage. *Adv. Energy Mater.* **2019**, *9*, 1900145. [CrossRef]
37. Sun, T.; Wang, J.; Chi, X.; Lin, Y.; Chen, Z.; Ling, X.; Qiu, C.; Xu, Y.; Song, L.; Chen, W.; et al. Engineering the Electronic Structure of MoS_2 Nanorods by N and Mn Dopants for Ultra-Efficient Hydrogen Production. *ACS. Catal.* **2018**, *8*, 7585–7592. [CrossRef]
38. Huang, H.; Huang, W.; Yang, Z.; Huang, J.; Lin, J.; Liu, W.; Liu, Y. Strongly coupled MoS_2 nanoflake–carbon nanotube nanocomposite as an excellent electrocatalyst for hydrogen evolution reaction. *J. Mater. Chem. A* **2017**, *5*, 1558–1566. [CrossRef]
39. Rasamani, K.D.; Alimohammadi, F.; Sun, Y. Interlayer-expanded MoS_2. *Mater. Today* **2017**, *20*, 83–91. [CrossRef]
40. Xu, J.; Zhang, J.; Zhang, W.; Lee, C.S. Interlayer nanoarchitectonics of two-dimensional transition-metal dichalcogenides nanosheets for energy storage and conversion applications. *Adv. Energy. Mater.* **2017**, *7*, 1700571. [CrossRef]
41. Wang, A.; Zheng, Z.; Wang, H.; Chen, Y.; Luo, C.; Liang, D.; Hu, B.; Qiu, R.; Yan, K. 3D hierarchical H_2-reduced Mn-doped CeO_2 microflowers assembled from nanotubes as a high-performance Fenton-like photocatalyst for tetracycline antibiotics degradation. *Appl. Catal. B* **2020**, *277*, 119171. [CrossRef]
42. Rout, C.S.; Khare, R.; Kashid, R.V.; Joag, D.S.; More, M.A.; Lanzillo, N.A.; Washington, M.; Nayak, S.K.; Late, D.J. Metallic few-layer flowerlike VS_2 Nanosheets as field emitters. *Eur. J. Inorg. Chem.* **2014**, *2014*, 5331–5336. [CrossRef]
43. Yang, M.; Li, J.X.; Li, H.H.; Su, L.W.; Wei, J.P.; Zhou, Z. Mesoporous slit-structured NiO for high-performance pseudocapacitors. *Phys. Chem. Chem. Phys.* **2012**, *14*, 11048–11052. [CrossRef] [PubMed]
44. Huang, B.; Bartholomew, C.H.; Woodfield, B.F. Improved calculations of pore size distribution for relatively large, irregular slit-shaped mesopore structure. *Microporous Mesoporous Mater.* **2014**, *184*, 112–121. [CrossRef]
45. Singal, S.; Joshi, A.; Singh, G.; Sharma, R.K. Dual approach of antimonene hybridization and hierarchical structuration to expose more active sites for improved charge storage characteristics of VS_4. *J. Power Sources* **2020**, *475*, 228669. [CrossRef]
46. Wang, J.; Zheng, X.; Dong, Y.; Chen, L.; Chen, L.; He, W. Reactant conversion–intercalation strategy toward interlayer-expanded MoS_2 microflowers with superior supercapacitor performance. *Dalton Trans.* **2023**, *52*, 4537–4547. [CrossRef] [PubMed]
47. Lu, W.; Yuan, Z.; Xu, C.; Ning, J.; Zhong, Y.; Zhang, Z.; Hu, Y. Construction of mesoporous Cu-doped Co9S8 rectangular nanotube arrays for high energy density all-solid-state asymmetric supercapacitors. *J. Mater. Chem. A* **2019**, *7*, 5333–5343. [CrossRef]
48. Tang, H.; Wang, J.; Yin, H.; Zhao, H.; Wang, D.; Tang, Z. Growth of polypyrrole ultrathin films on MoS_2 monolayers as high-performance supercapacitor electrodes. *Adv. Mater.* **2015**, *27*, 1117–1123. [CrossRef]
49. Cheng, J.; Lu, Z.; Zhao, X.; Chen, X.; Liu, Y. Green needle coke-derived porous carbon for high-performance symmetric supercapacitor. *J. Power Sources* **2021**, *494*, 229770. [CrossRef]
50. Wang, P.; Zhang, G.; Li, M.; Yin, Y.; Li, J.; Li, G.; Wang, W.; Peng, W.; Cao, F.; Guo, Y. Porous carbon for high-energy density symmetrical supercapacitor and lithium-ion hybrid electrochemical capacitors. *Chem. Eng. J.* **2019**, *375*, 122020. [CrossRef]
51. Thakur, A.K.; Choudhary, R.B.; Majumder, M.; Gupta, G.; Shelke, M. Enhanced electrochemical performance of polypyrrole coated MoS_2 nanocomposites as electrode material for supercapacitor application. *J. Electroanal. Chem.* **2016**, *782*, 278–287. [CrossRef]
52. Li, X.; Li, X.; Cheng, J.; Yuan, D.; Ni, W.; Guan, Q.; Gao, L.; Wang, B. Fiber-shaped solid-state supercapacitors based on molybdenum disulfide nanosheets for a self-powered photodetecting system. *Nano Energy* **2016**, *21*, 228–237. [CrossRef]
53. Ali, B.A.; Omar, A.M.A.; Khalil, A.S.G.; Allam, N.K. Untapped Potential of Polymorph MoS_2: Tuned Cationic Intercalation for High-Performance Symmetric Supercapacitors. *ACS Appl. Mater. Interfaces* **2019**, *11*, 33955–33965. [CrossRef]
54. Acerce, M.; Voiry, D.; Chhowalla, M. Metallic 1T phase MoS_2 nanosheets as supercapacitor electrode materials. *Nat. Nanotechnol.* **2015**, *10*, 313–318. [CrossRef]
55. Oyedotun, K.O.; Barzegar, F.; Mirghni, A.A.; Khaleed, A.A.; Masikhwa, T.M.; Manyala, N. Examination of high-porosity activated carbon obtained from dehydration of white sugar for electrochemical capacitor applications. *ACS Sustain. Chem. Eng.* **2018**, *7*, 537–546. [CrossRef]

56. Ji, Y.; Wei, Q.; Sun, Y. Superior Capacitive Performance Enabled by Edge-Oriented and Interlayer-Expanded MoS_2 Nanosheets Anchored on Reduced Graphene Oxide Sheets. *Ind. Eng. Chem. Res.* **2018**, *57*, 4571–4576. [CrossRef]
57. Nandana, A.B.; Rakhi, R.B. Exploring Vanadium Disulfide (VS_2) Nanosheets as High Efficiency Supercapacitor Electrodes. *Energy Technol.* **2025**, *13*, 2402153. [CrossRef]

Disclaimer/Publisher's Note: The statements, opinions and data contained in all publications are solely those of the individual author(s) and contributor(s) and not of MDPI and/or the editor(s). MDPI and/or the editor(s) disclaim responsibility for any injury to people or property resulting from any ideas, methods, instructions or products referred to in the content.